



## Chirp sub-bottom profiler source signature design and field testing

Martin Gutowski<sup>1,\*</sup>, Jon Bull<sup>1</sup>, Tim Henstock<sup>1</sup>, Justin Dix<sup>1</sup>, Peter Hogarth<sup>2</sup>, Tim Leighton<sup>3</sup> & Paul White<sup>3</sup>

<sup>1</sup>*School of Ocean and Earth Sciences, Southampton Oceanography Centre, European Way, Southampton, SO14 3ZH, United Kingdom; mxg@soc.soton.ac.uk*

<sup>2</sup>*GeoAcoustics Ltd., Shuttleworth Close, Gapton Hall Industrial Estate, Great Yarmouth, Norfolk, NR31 0NQ, United Kingdom*

<sup>3</sup>*Institute of Sound and Vibration Research, Southampton University, Highfield, Southampton, SO17 1BJ, United Kingdom; \*Author for correspondence (Phone: ++44 (0)23 80596488; Fax: ++44 (0)23 80593052; E-mail: M.Gutowski@soton.ac.uk)*

**Key words:** chirp, high-resolution seismics, marine seismics, reflection seismics, seismic sources

### Abstract

Chirp sub-bottom profilers are marine sonar systems which use a highly repeatable source signature to facilitate the acquisition of correlated data with decimetre vertical resolution in the top 20–30 m of sediments. Source signatures can be readily developed and implemented, but an applicable methodology for assessing resolution and attenuation characteristics of these wide-band systems did not exist. Methodologies are developed and applied to seven contrasting source signatures which occupy the same frequency band, but differ in their Envelope and Instantaneous Frequency functions. For the Chirp source signatures tested, a Sine-Squared envelope function is shown to produce seismic data with the optimum resolution and penetration characteristics.

### Introduction

The chirp systems described in this paper are marine wide-band, frequency-modulated, sub-bottom profilers that produce high-quality, high-resolution, normal incidence seismic reflection data. They comprise calibrated, linear electronics that are capable of producing a highly repeatable source signature (Schock and LeBlanc, 1990). They transmit a frequency modulated (FM) signal that is corrected for the source and receiver phase and amplitude responses. Owing to the wide bandwidth of the signal, optimum penetration, as well as, resolution can be achieved. The signal-to-noise-ratio (SNR) is improved through matched filter processing by correlating the reflection data with the transmitted pulse. Chirp systems typically operate within a range of 400 Hz–24 kHz and offer a vertical resolution on a decimetre scale in the top c. 20–30 m of unconsolidated sediments. Chirp sub-bottom profilers have been widely used for geological/geophysical (e.g. Quinn et al., 1997a; Jakobsson,

1999), geo-technical (e.g., Selby and Foley, 1995; Kim et al., 1999) and archaeological projects (e.g. Quinn et al., 1997b; Bull et al., 1998). Quinn et al. (1997c) proposed a processing flow to optimise the imaging of chirp data.

The land analogue of the Chirp systems described previously, albeit much lower frequency, typically below 1 kHz, is the Vibroseis mechanical vibrator technique. One of the main concerns with land swept frequency systems is validation of the form of the pulse actually transmitted into the sub-surface. Validation of Chirp source signatures is much more straightforward, and is commonly completed in water-filled test tanks where the reflection from the base of the tank is used to calibrate the system. There has been some work completed on Vibroseis and Chirp source signatures, which is summarised below.

Goupillaud (1976) investigated sweeps for the Vibroseis system and discussed sweeps with a constant amplitude function but varying Instantaneous Frequency Function (IFF). He studied the difference

between sweeps with linear and non-linear IFFs, referred to here as linear and non-linear sweeps. He concluded that a non-linear sweep could be viewed as a filter which controlled the spectrum shapes, and that the use of such a sweep is equivalent to the use of a linear sweep with successive filtering provided that the earth resembles a linear filter. Although Goupillaud found that this is approximately true for the frequency range of 12–75 Hz of the investigated sweeps, this might not be true for high frequency, wider bandwidth sweeps. Additionally he presented one experimental example which showed some differences between the non-linear and the filtered linear sweep.

The influence of the Envelope function for linear sweeps on the auto-correlation function was investigated by Cunningham (1979). He points out that by using an Envelope function the correlation side-lobes of the correlated signal could be significantly reduced. However, the use of Envelope functions led to a reduction of energy output and reduced the bandwidth of the signal, resulting in a wider main-lobe of the correlation function and a reduced spatial resolution.

Schock et al. (1994) suggested a linear sweep for a chirp system with a Blackman-Harris envelope shape (Harris, 1978) for the use in Chirp systems. These authors point out that such a sweep would have a very low side-lobe level. Moreover they showed that the sweep maintains its bandwidth and shape when attenuated with a linear frequency dependency, experiencing only a decrease in amplitude. Additionally, if a non-linear attenuation for seafloor sediments (such as that demonstrated by Jacobson, 1987 and Hamilton, 1980) occurs, then the loss in bandwidth and the resulting widening of the autocorrelation function of the sweep, known as the Klauder wavelet, are relatively small compared to sweeps with other Envelope functions.

The advantage of being able to control precisely the source signature is that the source sweep used can be optimised according to survey task, and the vertical resolution and penetration characteristics required. In order to discriminate quantitatively between different source signatures, a methodology needs to be developed to provide useful data on *relative* vertical resolution and rate of attenuation. In the literature there is a lack of quantitative comparison of chirp source signatures, and the aims of this paper are to provide a methodology for this analysis, and to provide a data set to explore optimisation.

This paper presents a number of newly developed source sweeps that differ in their Envelope and Instantaneous Frequency functions. The sweeps were used in

sea trials off the north coast of the Isle of Wight (UK) in which a 1.2 km long seismic profile was repeatedly measured with different source sweeps. The sections are analysed for their resolution and attenuation, and compared with theoretical predictions.

## Sweep design

This work examines the seven different source sweeps listed in Table I. Figures 1–7 summarise the characteristics of each sweep detailing, in each case, (a) the time domain representation; (b) the amplitude spectrum; (c) the spectrogram which shows the variation in spectral content with time on a dB scale, revealing the sweeps Instantaneous Amplitude function; and (d) the Klauder wavelet. The different source sweeps were generated by changing three attributes: the frequency content, the IFF, and the Envelope function. The transducer frequency response (transducer model T135 Neptune Sonar Ltd.) allows the frequency content of the sweep to be in the range 1.5–13 kHz. The IFF details how the frequency content changes over the length of the sweep; here linear, quadratic and logarithmic functions are used. The Envelope function defines the variation with amplitude with time, and in this study Blackmann-Harris, Gaussian, Chi, reversed Chi, and Sine-Squared functions are tested. The newly developed sweeps were compensated for the transducer's frequency response, which had been determined in test-tank experiments, before integrating them into the system.

Sweeps S1 and S2 (Figures 1 and 2) are widely used in commercial Chirp systems, and use a Blackmann-Harris Envelope function and linear IFFs, with S2 having wider bandwidth and mean frequency (c.f. Table I). These two 'traditional' sweeps will be used as a reference for comparison with the newly generated sweeps. Unlike these conventional signals, all of the new sweeps utilise the full bandwidth of the transducers.

Three different sweeps, all with relatively low mean frequency and asymmetric spectra are detailed in Figures 3–5. For Sweep S3 (Figure 3) the relatively low mean frequency and asymmetric spectrum is produced using a quadratic IFF, which causes more time to be spent at lower frequencies, and a Gaussian Envelope function. Sweep S4 (Figure 4) was produced using a reversed Chi function giving high amplitudes at high frequencies, but with a logarithmic IFF with long duration at low frequencies. A Chi Envelope

Table 1. A summary of the characteristics of the source sweeps examined.

Sweep	Frequency range [kHz]	Envelope function	IFF	−3 dB amplitude bandwidth [kHz]	$f_{\text{mean}}$ [kHz]
s1	2–8	Blackmann-Harris	linear	1,72	4,50
s2	1.5–11.5	Blackmann-Harris	linear	3,38	6,50
s3	1.5–13	Gauss	quadratic	2,54	4.48
s4	1.5–13	Chi reversed	logarithmic	1,94	3.25
s5	1.5–13	Chi	linear	2,66	4.30
s6	1.5–13	sine-squared 4th	linear	7,82	7.25
s7	1.5–13	sine-squared 8th	linear	9,65	7.25

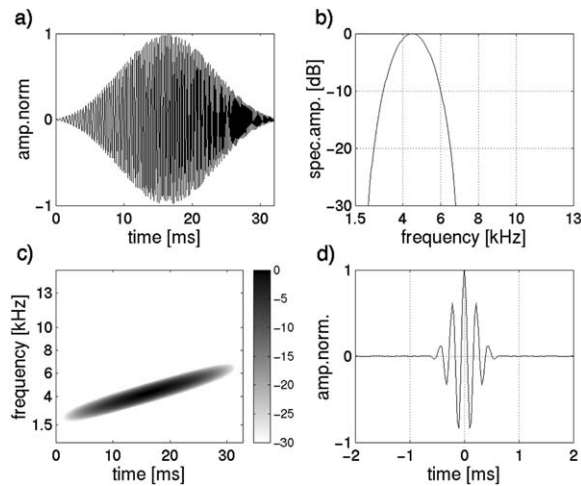


Figure 1. Source sweep S1. Standard linear low frequency sweep with Blackmann-Harris Envelope function. a) Time domain representation. b) Power spectrum with a mean frequency of 4.5 kHz. c) Spectrogram showing the linear IFF. The greyscale represents the same dB scale as in the spectrum. d) Klauder wavelet, the normalised auto-correlation function of the sweep.

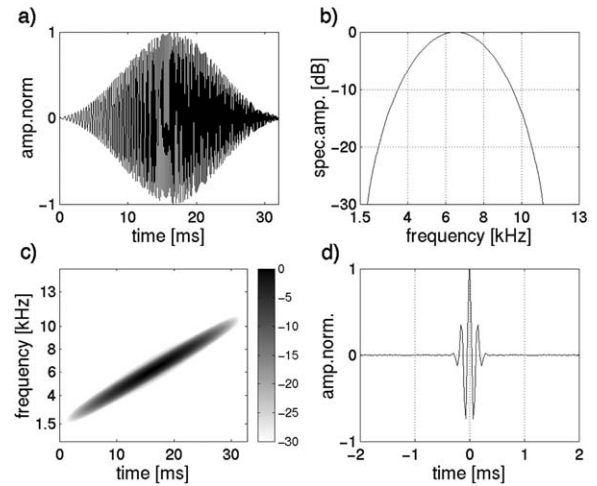


Figure 2. Source sweep S2. Standard linear high frequency sweep with Blackmann-Harris Envelope function. a) Time domain representation. b) Power spectrum with a mean frequency of 6.5 kHz. c) Spectrogram showing the linear IFF. The greyscale represents the same dB scale as in the spectrum. d) Klauder wavelet, the normalised auto-correlation function of the sweep.

function, with relatively high amplitudes at low frequencies, and a linear IFF was used to produce sweep S5 (Figure 5). For the linear sweeps S6 and S7 (Figures 6 and 7) a sine-squared taper function was used to optimise the power output over the frequency range while suppressing correlation side-lobes. For sweep S6 the sine-square taper covers half the duration of the waveform, for sweep S7 it covers a quarter of the duration.

## Experiment

Sea trials were undertaken in the West Solent off the north coast of the Isle of Wight (UK) in which the

same seismic line was repeatedly recorded using different source sweeps. The survey area is shown in Figure 8a. A source catamaran housing a quadratic array of four source transducers was used together with a seismic streamer with a hydrophone group consisting of eight elements towed behind the source catamaran (Figure 8b). Sweeps could be selected and changed on-board the survey vessel without the need to retrieve the source catamaran. The single channel seismic data were recorded with a shot interval of 250 ms together with Differential GPS navigational data.

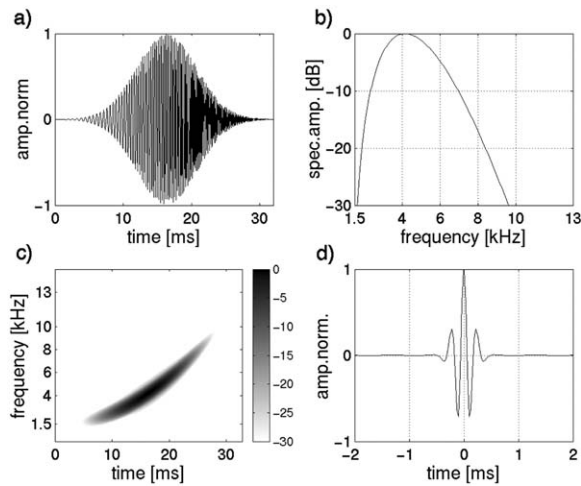


Figure 3. Source sweep S3. Quadratic sweep with Gaussian Envelope function. a) Time domain representation. b) Power spectrum with a mean frequency of 4.48 kHz. c) Spectrogram showing the quadratic IFF. The greyscale represents the same dB scale as in the spectrum. d) Klauder wavelet, the normalised auto-correlation function of the sweep.

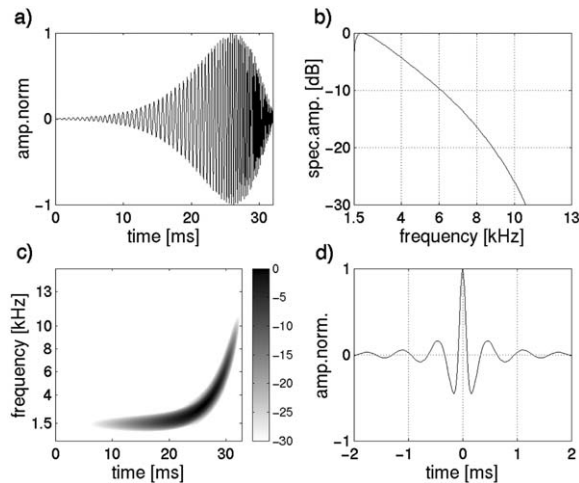


Figure 4. Source sweep S4: Logarithmic sweep with Chi reversed Envelope function. a) Time domain representation. b) Power spectrum with a mean frequency of 3.25 kHz. c) Spectrogram showing the logarithmic IFF. The greyscale represents the same dB scale as in the spectrum. d) Klauder wavelet, the normalised auto-correlation function of the sweep.

## Seismic sections

Figure 9 shows seismic sections of part of the repeatedly surveyed seismic line recorded with the different source sweeps. The horizontal axis displays the distance from the start of each line section. All the profiles are 650 m long, with the exception of Figure 9f where the profile is truncated at the south-west end.

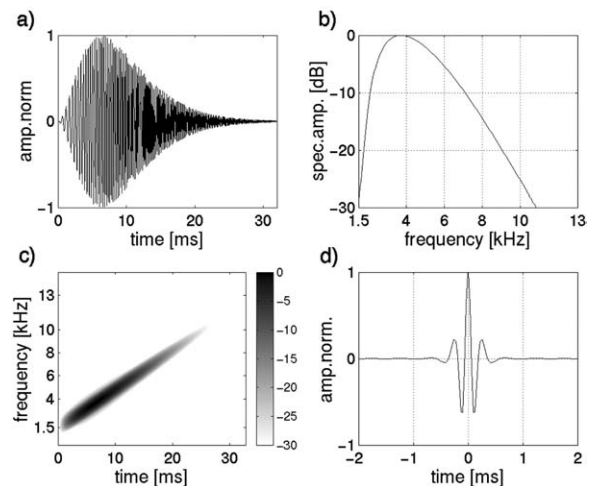


Figure 5. Source sweep S5 Linear sweep with Chi Envelope function. a) Time domain representation. b) Power spectrum with a mean frequency of 4.3 kHz. c) Spectrogram showing the linear IFF. The greyscale represents the same dB scale as in the spectrum. d) Klauder wavelet, the normalised auto-correlation function of the sweep.

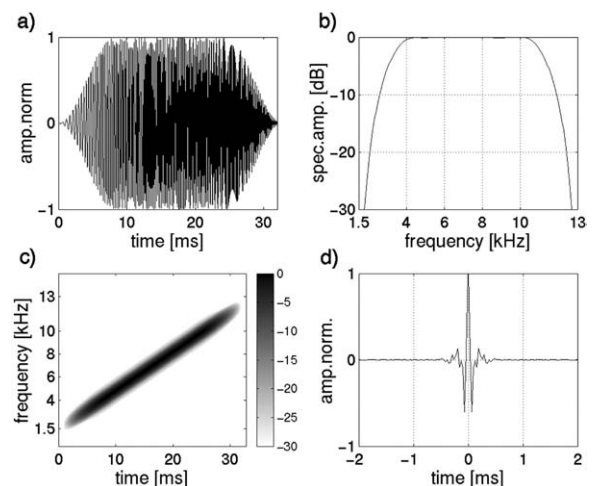


Figure 6. Source sweep S6. Linear sweep with sine-squared taper function, covering 1/4<sup>th</sup> of the time duration. a) Time domain representation. b) Power spectrum with a mean frequency of 7.25 kHz. c) Spectrogram showing the linear IFF. The greyscale represents the same dB scale as in the spectrum. d) Klauder wavelet, the normalised auto-correlation function of the sweep.

The sections image the folded Tertiary Bembridge Limestone and Bouldnor formations, which comprise limestones and shales (Daley et al., 1979). The variations in the structures imaged on the seismic profiles are due to variations in navigation between the profiles shown in Figure 9h. Note that line S1, showing the strongest variation in the imaged structures, has an offset of up to 30 m to the other lines. The seis-

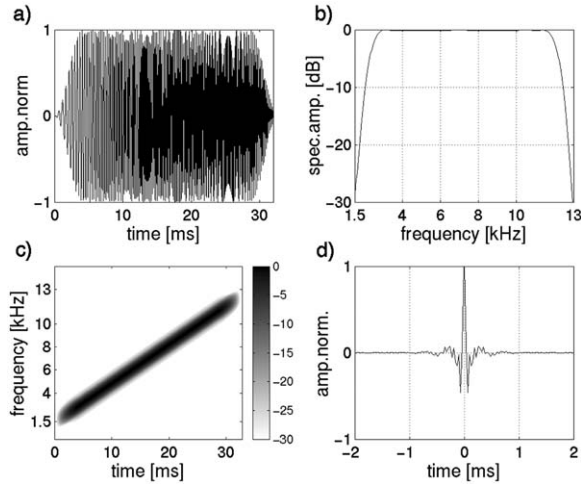


Figure 7. Source sweep S7. Linear sweep with sine squared taper function, covering  $1/8^{\text{th}}$  of the time duration. a) Time domain representation. b) Power spectrum with a mean frequency of 7.25 kHz. c) Spectrogram showing the linear IFF. The greyscale represents the same dB scale as in the spectrum. d) Klauder wavelet, the normalised auto-correlation function of the sweep.

mic data were processed using a flow described by Quinn et al. (1997(c)) including bandpass filtering, Instantaneous Amplitude calculation, f-x deconvolution, dynamic signal to noise filtering and automatic gain control. The same parameters were used for each data-set with a different bandpass filter applied within the limits of the frequency range of the sweeps (c.f. Table I). The areas used later for the quantitative comparison of attenuation and vertical resolution are highlighted, although for the qualitative comparisons, the entire sections are taken into account. Figure 9i shows the raw correlated data for sweep S1 of the highlighted area in Figure 9a. The raw data is included to indicate clearly the reflection events used for quantitative analysis, and to demonstrate the improvement in the interpretability of the processed sections. The seafloor multiple reflection present at about 40 ms two-way-travel time (TWT) prevents the imaging of deeper structures, although for some data-sets primary events can be traced below the multiple reflection. The general data quality varies within and between the sections owing to source and receiver movements, which were dependent on the changing tidal currents. Generally the lines recorded running against the tidal current are less noisy (sweeps S1, S4, S5, S7), but this did not affect our analysis.

Major differences are apparent when comparing the sections for the relatively low mean frequency sweeps (S1 and S3-S5). Sweeps S3 and S5 show

tighter reflection horizons compared to sweeps S1 and S4. This is especially apparent when comparing the pronounced reflector in the south-western part of the section (reflector at ca. 40 ms TWT within each boxed area on Figure 9). Some reflection horizons north-east of 500 m along each profile can be interpreted which are not visible for S1. In the section for sweep S4 (Figure 9d at 450 m) some reflectors can be traced beyond the seafloor multiple reflection suggesting lower loss of amplitude for this sweep.

Comparing the sections with the relatively higher mean frequency sweeps (S2, S6 and S7) it is apparent that they strongly differ in their noise content, with S2 and S6 being much noisier than S7. However, the sections for the sweeps S6 and S7 show slightly tighter reflections compared to S2, and this is especially apparent north-east of 500 m along each section where there is a lower noise level. Section S7 shows the greatest resolution of all the sections. In some places (e.g., 525 m along section at ca. 25 ms TWT) two separate reflection horizons can be interpreted, where in other sections only one horizon is visible.

## Data analysis

### Resolution

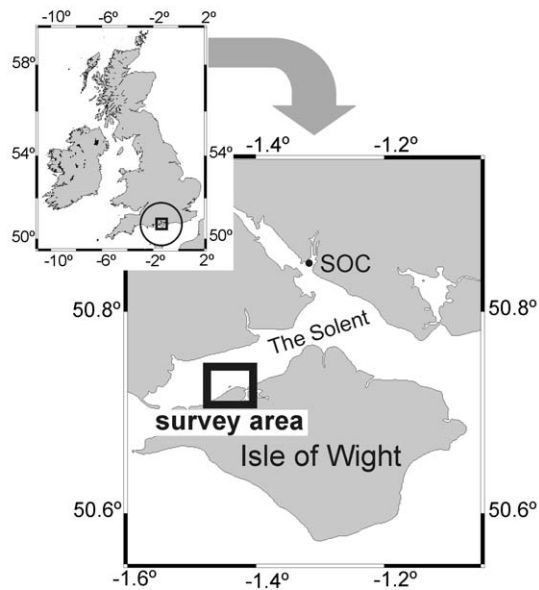
The vertical resolution of a chirp sweep is controlled by the width of its Klauder wavelet, which is approximately equal to the inverse of the source bandwidth. Comparing the newly developed sweeps (S3-S7), they have the same frequency range, but vary significantly in their spectra, their  $-3$  dB bandwidth (c.f. Table I) and therefore in the shape of the Klauder wavelet. The characteristics of the Klauder wavelets can be compared in more detail by calculating the integral amplitude build-up of the Klauder wavelet  $A(t_{int})$ , which is given as

$$A(t_{int}) = \int_{t_0}^{t_{int}} |s(t)| \cdot dt, \quad (1)$$

where  $t_{int}$  is the integration time,  $t_0$  is the start time of the integration and  $s(t)$  is the Klauder wavelet. This time domain analysis quantifies the energy distribution within the Klauder wavelet.

To facilitate a comparison of theoretical and experimental data, the same start time  $t_0$  was chosen for the amplitude build-up calculation. Although the calculation of the amplitude build-up of the theoretical Klauder wavelet,  $t_0$  can be chosen to be  $-\infty$ ,

a)



b)

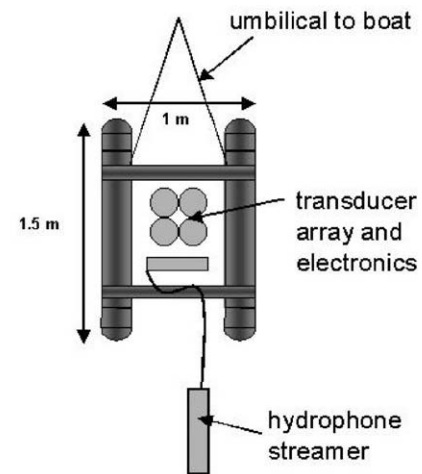


Figure 8. a) Survey area in the West Solent (UK) off the north coast of the Isle of Wight. The box shows the area in which a 1.2 km long seismic profile was repeatedly recorded using different chirp source sweeps. b) Plan view of Chirp sub-bottom profiler system used in the experiment. The source comprises a quadratic array of four transducer elements (Neptune Sonar Ltd.) located in a catamaran together with the controlling electronics. The receiver array consists of a group of 8 hydrophone elements within a 1 m streamer, which is towed 2 m behind the catamaran. The catamaran itself is towed at a distance of ca. 10 m behind the survey vessel to reduce the impact of engine noise and to ensure a stable towing behaviour.

due to the noisiness of the experimental data,  $t_0$  was set to be  $-1$  ms before the correlation maximum at a correlation lag-time  $t_{lag} = 0$ . The upper limit for the integration is the time at which the Klauder wavelet maximum occurs, which for the theoretical signal occurs when  $t_{lag} = 0$ . The best theoretical resolution would be expected from a signal whose amplitude build-up function is concentrated at  $t_{lag} = 0$ . The tighter the amplitude build-up curve towards  $t_{lag} = 0$ , the better the resolution capabilities of the source sweep. The analysis of the experimental data was carried out before the data was processed as described above.

Figure 10 shows the normalised theoretical amplitude build-up functions for the source sweeps examined. The shape of the respective Klauder wavelet controls the form of each curve: the undulations in the amplitude functions correspond to the side-lobes of the wavelet; the time at which the amplitude function starts increasing corresponds with the time duration of the wavelet. The steeper the ascent towards  $t_{lag} = 0$  the tighter the main-lobe of the Klauder wavelet. Comparing the sweeps with relatively low mean frequency shows that S4 has the widest am-

plitude build-up curve and a low ascent rate owing to the wide main-lobe and wide primary side-lobes together with a slow decay of the side-lobe amplitudes of the Klauder wavelet. Sweeps S3 and S5 show similar, relatively tight curves due to fast decay of side-lobe amplitudes and tight primary side-lobes. The curve for S1 is wider compared to S4 and S5 owing to high amplitude primary side-lobes. Comparing the sweeps with a higher mean frequency shows that the amplitude build-up curves for sweeps S6 and S7 have a very steep ascent compared to S2 due to a very tight main-lobe of the Klauder wavelet. Owing to the slower decay of the side-lobe amplitudes, the curves for S6 and S7 are broad, compared to S2, with S7 showing the fastest amplitude accumulation, because its Envelope Function is most similar to a box function.

To facilitate a quantitative comparison, the time duration from the half amplitude build-up to the full build-up ( $t_{lag} = 0$ ) can be used to compare the resolution capabilities of the sweeps. Time durations were calculated for the theoretical, as well as for the experimental data. The experimental values were computed from the amplitude build-up curves for seafloor reflec-

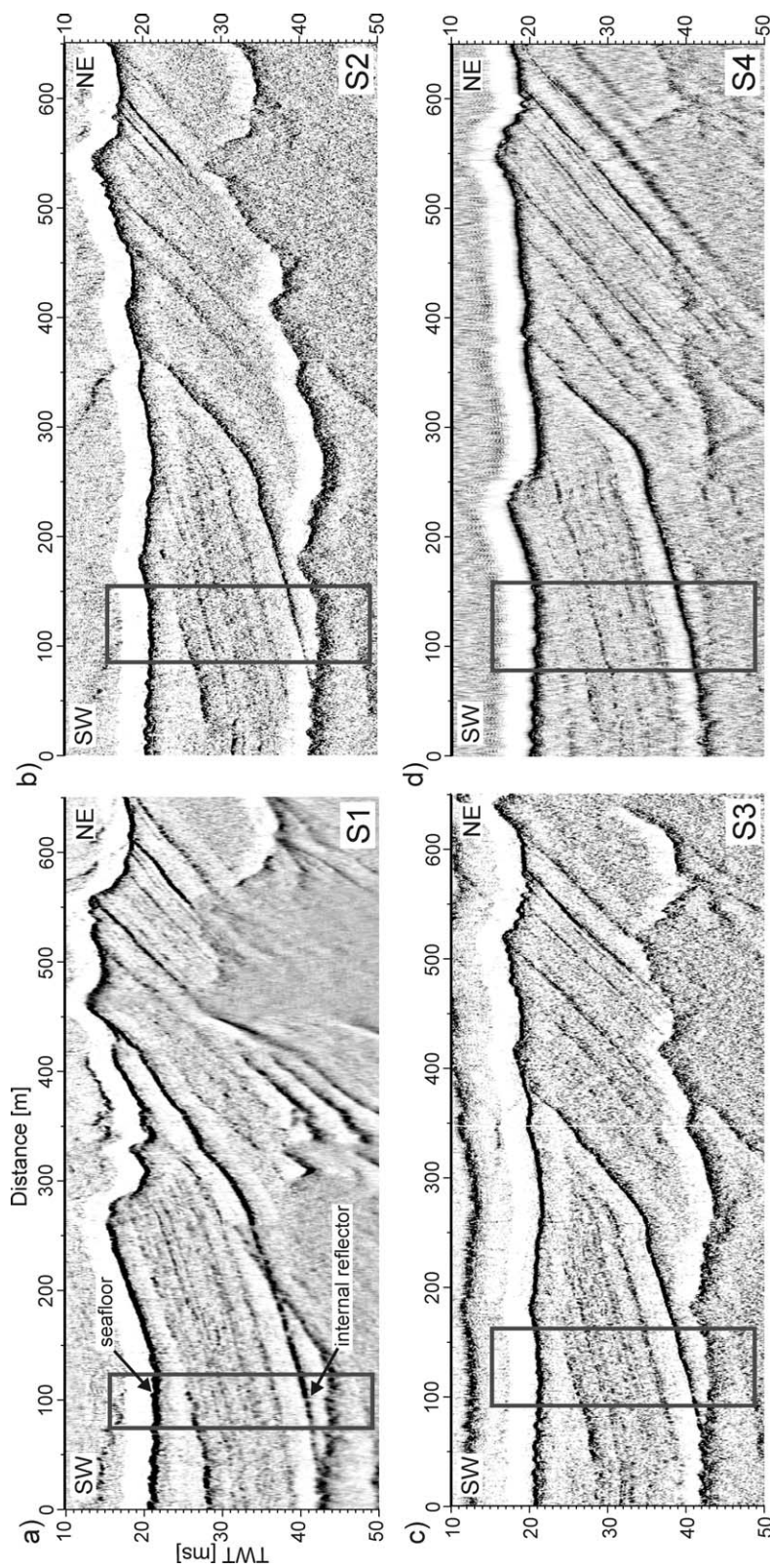


Figure 9.1. a)-g) Seismic sections recorded in the area in the West Solent (UK) (c.f. Figure 8). h) Plot of the navigational data for the seismic lines. i) Raw correlated data from sweep S1 from highlighted area in a). Note the seafloor and internal reflection events used in the analysis. The seismic data was processed using a flow described by Quinn et al. (1997(c)) comprising bandpass filtering, Instantaneous Amplitude calculation, f-x deconvolution, dynamic signal to noise filtering and automatic gain control. a) Sweep S1. Standard linear low frequency sweep with Blackmann-Harris Envelope function. b) Sweep S2. Standard linear high frequency sweep with Blackmann-Harris Envelope function. c) Sweep S3. Quadratic sweep with Gaussian Envelope function. d) Sweep S4. Logarithmic sweep with Chi reversed Envelope function. e) Sweep S5. Linear sweep with Chi Envelope function. f) Sweep S6. Linear sweep with sine-squared taper function, covering  $1/4^{\text{th}}$  of the time duration. g) Sweep S7. Linear sweep with sine-squared taper function, covering  $1/8^{\text{th}}$  of the time duration. The sections image Tertiary limestones and shales, see main text for details.

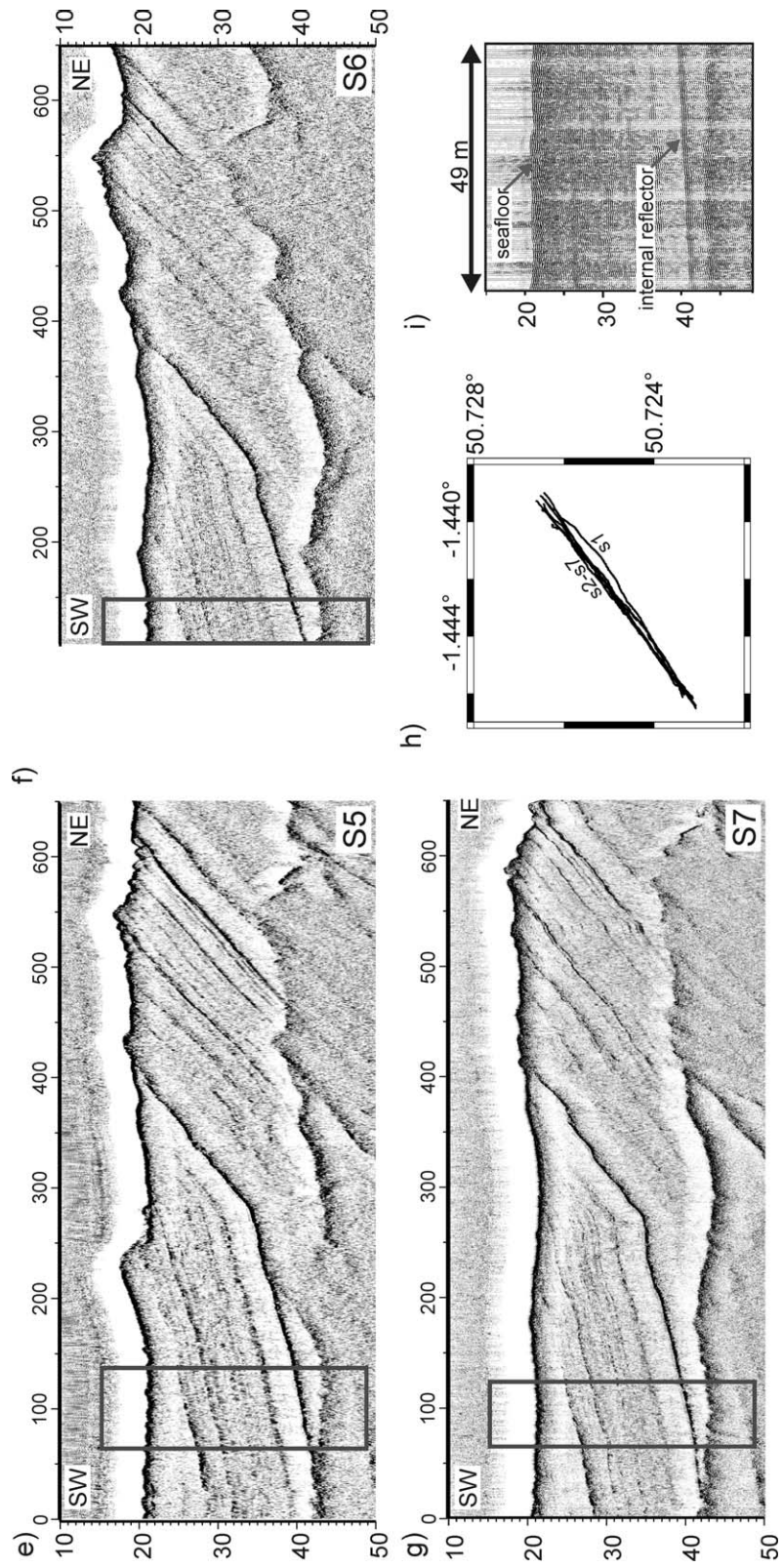


Figure 9.2. Continued.



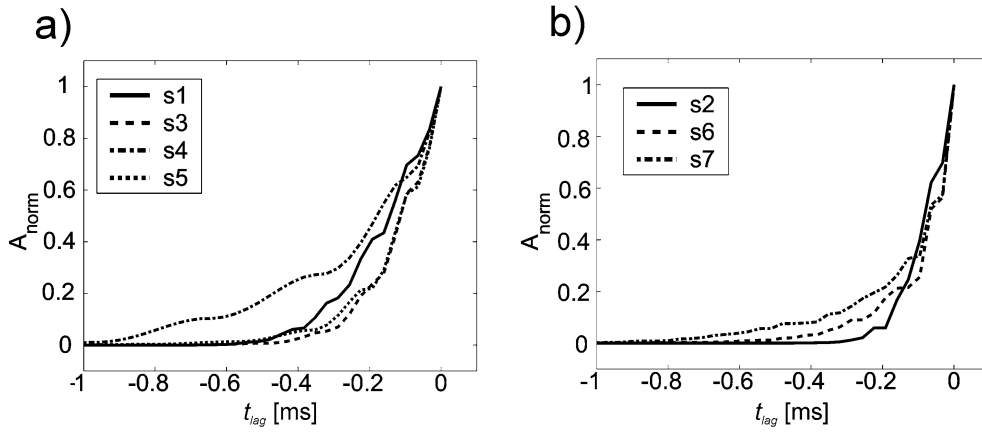


Figure 10. Normalised amplitude build-up curves of the examined source sweeps. a) Low mean frequency sweeps S1, S3, S4 and S5. b) High mean frequency sweeps S2, S6 and S7. The curves comprise the evaluation of (1) with integration limits of  $t_{lag} = -1$  ms to  $t_{lag} = 0$  ms.

Table 2. Analysis of attenuation ( $a_{app}$ ) and time duration from the half amplitude build-up to the full build-up for the Klauder wavelet expected from theory, and from experiment, for each sweep. The stated errors are standard deviation errors calculated for the experimental results.

Sweep	$f_{mean}$ [kHz]	Amplitude build-up half-width [ms]			$a_{app}$ [dB/m]		
		Theory	Data	$\pm$	Model	Data	$\pm$
s1	4,50	0,143	0,143	0,007	0,29	0,38	0,13
s2	6,50	0,081	0,097	0,020	0,59	0,63	0,15
s3	4,48	0,113	0,127	0,023	0,29	0,38	0,12
s4	3,25	0,180	0,224	0,012	0,16	0,25	0,17
s5	4,30	0,114	0,119	0,016	0,27	0,38	0,18
s6	7,25	0,066	0,070	0,015	0,71	0,64	0,18
s7	7,25	0,070	0,088	0,030	0,70	0,56	0,19

tions in the highlighted area of the seismic sections shown in Figure 9. The values are listed in Table II.

Figure 11 plots the time duration from the half amplitude build-up to the full build-up for both theoretical and experimental data for each sweep examined (a), and against the mean frequency of each sweep (b). The theoretical and experimentally-derived measurements agree within error, except for sweep S4. The experimental half-width values are systematically higher than the theoretical. This is a result of the presence of ambient noise, which causes temporal widening of the build-up curves. The experimental data for sweep S4 has a relatively noisy seafloor reflection signal, which explains the discrepancy.

Comparing the newly developed low mean frequency sweeps (c.f. Table II) S3, S4 and S5 with the ‘traditional’ sweep S1, shows that S3 and S5 both have a theoretical half-width value with temporal dur-

ation approximately 25% lower than S1, while S4 has an increased temporal duration ca. 25% more than S1. From this analysis sweeps S3 and S5 would be expected to offer improved resolution, while having similar mean frequency. S4 has substantially lower mean frequency (38% lower than S1), while its resolution capabilities is reduced by 25%, based on the theoretical amplitude half-width.

The newly developed high mean frequency sweeps S6 and S7 all have smaller half-widths values than their ‘traditional’ counterpart S2 (23% and 17% respectively, from the theoretical amplitude build-up curves) and should enable enhanced resolution. Some of this improvement can be attributed to an increase in the mean frequency of the new sweeps (12% higher).

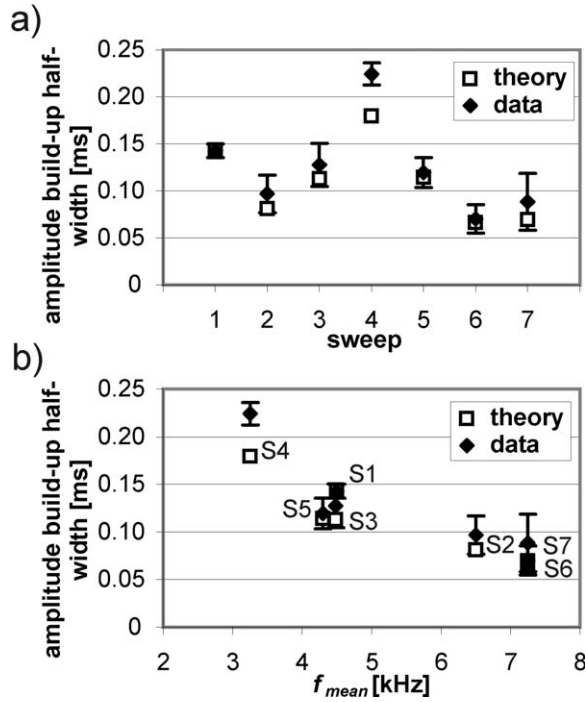


Figure 11. Half amplitude build-up widths for examined theoretical sweeps and extracted from the seafloor reflections in the highlighted area of the seismic sections shown in Figure 9. a) Plotted against sweep label. b) Plotted against the sweeps mean frequency.

#### Attenuation

To study the attenuation of the different source sweeps, seafloor reflection amplitudes are now compared with the amplitudes of a pronounced internal reflection horizon (see Figure 9). The reflection amplitude is dependent on the attenuation of the sweep between the respective horizons as a result of various mechanisms, as well as on the reflection coefficient of the horizons. As the reflection coefficients are not known an apparent attenuation is expressed, which includes the reflection coefficients and assumes that the attenuation is constant with depth. The apparent attenuation coefficient  $a_{app}$ , which depends on the frequency content of the used source sweep can be described as

$$a_{app}(\omega) = \frac{20}{z} \log \frac{R_1(\omega)}{R_0(\omega)}, \quad (2)$$

where  $R_0$  is the seafloor reflection amplitude,  $R_1$  the internal reflection amplitude,  $\omega$  angular frequency and  $z$  the depth between the two reflectors, assuming an average sediment velocity of 1800 m/s. It expresses the attenuation in units of dB/m. Before carrying out the calculation, an amplitude correction is applied, as-

suming spherical spreading. To compare the results of the different data sets, the same internal reflection horizons at the same depth interval are analysed, as shown in Figure 9. The area has been chosen to be homogenous with dipping reflectors to avoid amplitude alteration effects due to internal multiple reflections.

Additionally the attenuation of the sweeps was modelled using a model based on relaxation time as described by LeBlanc et al. (1991). The attenuated frequency domain signal  $Y(\omega)$  can be obtained by multiplying the signal in the frequency domain,  $S(\omega)$  with the frequency transfer function  $H(\omega)$

$$Y(\omega) = S(\omega)H(\omega), \quad (3)$$

which is given as

$$H(\omega) = e^{-(\alpha + jk)t}. \quad (4)$$

The real part of the exponent represents the attenuation of the sweep magnitude and for small frequencies (<100 kHz) the coefficient  $\alpha$  is given as

$$\alpha \approx \frac{\omega^2 \tau}{2}, \quad (5)$$

where  $\omega$  is the angular frequency of the signal and  $\tau$  the average relaxation time of the sediment, the measure of the finite time needed to change the density by application of a sudden pressure due to different mechanisms. The imaginary part of the exponent describes the time delay and phase dispersion of the signal and for small frequencies (<100 kHz) the coefficient  $k$  can be approximated by

$$k \approx \frac{\omega}{(1 + \frac{3}{8}\omega^2\tau^2)}. \quad (6)$$

The attenuated time domain signal is calculated by computing a Fast Fourier Transform (FFT), multiplying the signal with the frequency transfer function  $H(\omega)$  as described in (3) and lastly computing the inverse FFT. The apparent attenuation value is then calculated by comparing the amplitudes of the attenuated and original signal as described by (2). Since the relaxation time  $\tau$  is not known, this parameter is changed in the model to obtain the best least-square fit between model results and data for the entire data-set. A relaxation time of  $\tau = 0.135 \mu\text{s}$  produces the best fit. This is a typical value for coarse-grained marine sediments (LeBlanc et al., 1991).

Table II shows results of the calculations with standard deviation errors and the best least-squares fit model results. Figure 12 displays the experimental data and model results plotted against sweep (a), and against the mean frequency of the respective sweep

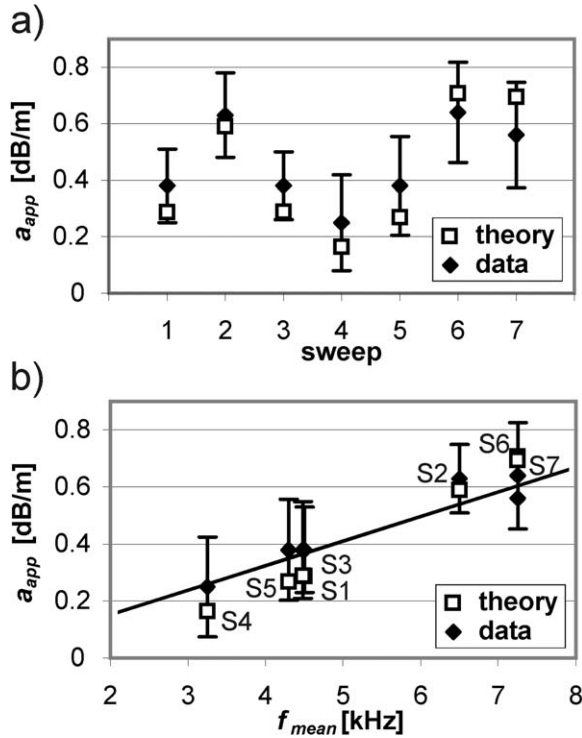


Figure 12. Experimental and modelled apparent attenuation values for the examined source sweeps. The experimental results were computed for the highlighted reflectors in the seismic sections shown in Figure 9. a) Plotted against sweep label. b) Plotted against the sweeps mean frequency. The best fit straight line corresponds to a quality factor  $Q = 169 \pm 56$ .

(b). Assuming that the intermediate reflection coefficients are negligible, and the velocity does not significantly increase with depth, an estimate for a constant quality factor  $Q$  can be obtained. The best-fit straight line for the experimental data in Figure 12b corresponds to a constant quality factor of  $Q = 169 \pm 56$ . This minimum bound estimate reflects the consolidated nature of the Tertiary stratigraphy, which facilitates sound propagation with relative low attenuation (Soloman, McCann and Sothcott, 1999; Dasios, Astin and McCann, 2001).

We have measured the attenuation within the sediment based on the different source sweeps. The measured results can be fit by both a relaxation time model and a constant  $Q$  model. In each case the results are similar to other estimates for marine sediments, however to unequivocally distinguish which method provides a better fit to the data would require a broader range of frequencies. Sweeps S2, S6, S7 are consistently more attenuated than the other sweeps, and sweep S4 is the least attenuated. Although not our

primary aim, the methodology described, that is using data acquired with different source sweeps with a wide range of mean frequencies, can be used to estimate the relaxation time and the  $Q$  values.

## Discussion

The two main considerations for choosing a particular sweep for a specific survey task are vertical resolution and penetration. As discussed earlier, the length of the Klauder wavelet controls the vertical resolution, while the depth of penetration is controlled by the attenuation of the sweep as it propagates through the sub-surface. Here the vertical resolution and attenuation of each of the sweeps examined are discussed.

In this paper it was demonstrated that seismic reflection sections over the same ground (Figure 9) can be used to provide qualitative comparison of the vertical resolution for each sweep used. For quantitative analysis of vertical resolution, measurements of the time duration from the half amplitude build-up to the full build-up of the Klauder wavelet can be used (Figure 10 and Table II). There is excellent agreement, on a sweep-by-sweep comparison, between the vertical resolution observed on the seismic sections (as qualitatively judged by the 'interpretability' of the sections, and the imaging of additional horizons), and the quantitative approach. Comparing the low frequency sweeps (S1 and S3-5), sweeps S3 and S5 offer the shortest Klauder wavelet (the temporally fastest amplitude build-up, Table II), and also provided the seismic sections with greatest spatial resolvability. For the high frequency sweeps (S2, S6 and S7), sweeps S6 and S7 offer better vertical resolution as judged by both the seismic sections (Figure 9) and Klauder wavelet considerations. Sweeps S6 and S7 which have a sine-squared envelope function have broader bandwidth (for example at  $-3$  dB, see Table I) than sweep S1 with the Blackman-Harris envelope function, and this explains their better resolution capabilities.

The limited water-depths in the chosen survey area meant that the multiple reflection hampered analysis of attenuation from the seismic data. Despite this, the modelled and observed attenuation values agree within error (Figure 12). Sweep S4, which has the lowest apparent attenuation value (Table II), shows little change in the noise level with depth indicating low attenuation, and provided the imaging of the deepest reflectors observed on any of the seismic profiles (Figure 9).

The selection of the optimal sweep for a particular task is a compromise between resolution and penetration. Normally there is a reduction in the depth of penetration achieved when using higher resolution sweeps. Thus, the improvement in resolution offered by the high frequency 'Sine-Squared' sweeps (S6 and S7) compared to the 'traditional' high frequency sweep S2 is remarkable, given the absence of a major increase in attenuation. For the low frequency sweeps (S3 and S5) an improvement in resolution can also be observed, in comparison with the 'traditional' sweep S1. The modelled and observed attenuation values are very similar for these sweeps, thus achieving an overall improvement for the newly developed low frequency sweeps over the 'traditional' sweep.

## Conclusions

This paper reports on the development of a number of chirp source sweeps, which exploit the entire bandwidth of the transducer, but which differ in their envelope and IFFs. The sweeps were tested in a seismic reflection sea trial by recording the same profile with the different source sweeps. To compare the resolution capabilities of the sweeps, analysis was made of the amplitude build-up of the Klauder wavelet, calculated for the theoretical waveform and extracted from the data-sets. To compare the attenuation of the sweeps an apparent attenuation value was calculated from the data-sets, and modelled using a relaxation time based model. A comparison of the low and high mean frequency sweeps characteristics showed that the newly developed sweeps offer advantages over the 'traditional' sweeps as they improve the resolution capabilities, while having similar or better resistance to attenuation.

## Acknowledgements

The authors acknowledge support from the Engineering and Physical Sciences Research Council/Joint Grant Scheme (GR/R 12695/01) for this work, which was completed as part of a larger study on 3D Chirp imaging. The manuscript was significantly improved using the comments of two anonymous reviewers.

## References

- Bull, J. M., Quinn, R. and Dix, J. K., 1998, Reflection Coefficient Calculation from Marine High Resolution Seismic Reflection (Chirp) Data and Application to an Archaeological Case Study, *Mar. Geophys. Res.* **20**, 1–11.
- Cunningham, A. B., 1979, Some alternate vibrator signals, *Geophysics* **44**, 1901–1921.
- Daley, B., Edwards, N. and Insole, A. N., 1979, Lithostratigraphical nomenclature of the English Paleogene Successions, *Geological Magazine* **116**, 65–66.
- Dasios, A., Astin, T. R. and McCann, C., 2001, Compressional-wave Q estimation from full-waveform sonic data, *Geophys. Prospect* **49**, 353–373.
- Goupillaud, P. L., 1976, Signal Design in the 'Vibroseis'® Technique, *Geophysics* **41**, 1291–1304.
- Hamilton, E. L., 1980, Geoacoustic modeling of the seafloor, *J. Acoust. Soc. Am.* **68**(5), 1313–1340.
- Harris, F. J., 1978, On the use of windows for harmonic analysis with discrete Fourier transform, *Proceedings IEEE* **66**, 51–83.
- Jacobson, R. S., 1987, An investigation into the fundamental relationships between attenuation, phase dispersion, and frequency using seismic refraction profiles over the sedimentary structures, *Geophysics* **52**(1), 72–87.
- Jakobsson, M., 1999, First high-resolution chirp sonar profiles from the central Arctic Ocean reveal erosion of Lomonosov Ridge sediments, *Mar. Geol.* **158**, 111–123.
- Kim, G. Y., Kim, D. C., Park, S. C., Lee, G. H., 1999, Chirp (2–7 kHz) echo characters and geotechnical properties of surface sediments in the Ulleung Basin, the East Sea, *Geosciences Journal* **3**(4), 213–224.
- LeBlanc, L. R., Panda, S., Schock, S. G., 1991, Sonar attenuation modeling for classification of marine sediments, *J. Acoust. Soc. Am.* **91**(1), 116–126.
- Quinn, R., Bull, J.M. and Dix, J. K., 1997(a), Buried scour marks as indicators of paleo-current direction, *Mar. Geol.* **140**, 405–413.
- Quinn, R., Bull, J.M. and Dix, J. K., 1997(b), Imaging Wooden Artefacts using Chirp Sources, *Archaeol. Prospect.* **4**, 25–35.
- Quinn, R., Bull, J.M. and Dix, J. K., 1997(c), Optimal processing of marine high-resolution seismic reflection (Chirp) data, *Mar. Geophys. Res.* **20**, 13–20.
- Schock, S. G. and LeBlanc, L. R., 1990, Chirp Sonar: New Technology For Sub-Bottom Profiling, *Sea Technology* **31**(9), 35–43.
- Schock, S. G., LeBlanc, L. R. and Panda, S., 1994, Spatial and Temporal Pulse Design Considerations for a Marine Sediment Classification Sonar, *IEEE Journal of Oceanic Engineering* **19**(3), 406–415.
- Selby, I. And Foley, M., 1995, An application of chirp acoustic profiling: monitoring dumped muds at sea bed disposal sites in Hong Kong, *Journal of Marine Environmental Engineering* **1**(3), 247–261.
- Solomon, A., McCann, C., Sothcott, J., 1999, Attenuation of P- and S-waves in limestones, *Geophys. Prospect.* **47**, 359–392.